ICAS 2016

30th Congress of the International Council
of the Aeronautical Sciences
DCC, Daejeon, Korea ; September 25-30, 2016

DIRECT NUMERICAL SIMULATION OF DISTURBANCES IN A THREE-DIMENSIONAL HYPERSONIC NEAR-WALL FLOW OVER FLAT PLATE AND COMPRESSION CORNER

A. V. Novikov*,, I. V. Egorov****
***Moscow Institute of Physics and Technology (MIPT), Dolgoprudny, 141701, Russia**
****Central Aerohydrodynamic Institute (TsAGI), Zhukovsky, 140180, Russia**

Abstract

Propagation of three-dimensional (3D) disturbances through the flat plate boundary layer and 5.5-degree compression-corner near-wall flow at the freestream Mach number 5.373 is simulated numerically. 3D Navier–Stokes equations are solved using the in-house parallel solver "HSFlow" on a fine grid. The disturbances are generated by a suction-blowing actuator placed on the wall working short time or permanently, producing wave packets or wave trains. The disturbances evolving downstream excite unstable waves relevant to the first and/or second mode instability depending on the actuator frequency and location. The instabilities propagating through the separation region exhibit nontrivial behavior. The growth of unstable waves ultimately leads to nonlinear breakdown and "young" turbulent wedge is formed. These numerical simulations will help to setup and perform controlled experiments in wind tunnels as well as develop holistic models of transitional boundary layer at hypersonic speeds.

1 Introduction

The problem of laminar-turbulent transition (LTT) in hypersonic flows over bodies is one of the main tasks of high-speed aerodynamics. Since LTT leads to significant increases in heat transfer, reliable estimates of LTT locations are needed to predict the aero-thermal loads and surface temperatures. LTT also has a significant effect on the aerodynamic performance because of a substantial increase of the skin friction. In the case of low free-stream disturbances typical for flight conditions, the LTT includes the three main stages [1]: receptivity to external disturbances; growth of unstable modes (such as first and second Mack modes, cross flow instability and Görtler vortices); nonlinear breakdown of disturbances leading to the fully turbulent flow regime. Physical mechanisms relevant to these stages can be investigated experimentally or numerically.

For systematic investigations of linear and especially nonlinear stages of LTT, the "controlled" experiments are most suitable, where disturbances of known spectral content are introduced by an artificial actuator. However, relatively few experimental efforts of this type have been reported in the literature (see [2-9]). In direct numerical simulations (DNS) the complete Navier–Stokes equations are solved by proper numerical methods without making restrictions on the basic (unperturbed) flow and disturbance amplitudes. Therefore, DNS is well suited for a holistic modelling of the all LTT stages including nonlinear breakdown. In addition, as opposed to physical experiments, DNS gives full information about 3D disturbance field, which enables to identify and study in detail different LTT mechanisms. The rapid development of supercomputers make it feasible to conduct such numerical studies for relatively simple configurations like a flat plate and a cone at zero angle of attack [10-11], where the boundary layer is attached to the wall and the mean flow weakly depends on the streamwise and spanwise coordinates. However, in the majority of practical cases we are dealing

with transition in locally separated boundary layers. One of the typical configurations is a compression corner, where the interaction between the oncoming boundary layer and the adverse pressure gradient drastically modifies the mean-flow field.

In this paper we present some results of DNS of artificially excited 3D disturbances propagating through the near-wall flows over flat plate and 5.5 degree compression-corner at the freestream Mach number 5.373 and unit Reynolds number $\mathrm{Re}_{\infty,1} = 17.9 \times 10^6 \ \mathrm{m}^{-1}$. These flow parameters are relevant to the Hyper-X model tested in the NASA LaRC 20-Inch Mach 6 Air Tunnel [12]. The earlier stability and numerical studies under these free-stream conditions were performed for 2D [13, 14] and 3D disturbances [15, 16] on a 5.5 degree compression corner. The disturbances are introduced via forcing of suction–blowing type through a small hole on the wall. The 3D Navier-Stokes equations for unsteady compressible flows of viscous perfect gas are solved using the in-house solver "HSFlow" (High-Speed Flow). The solver implements a fully implicit finite-volume shock-capturing method with the second-order approximation in space and time on multi-block structured grids.

Features of instability development in the linear and nonlinear stages are revealed using visualizations of the 3D vertical structures and wall pressure disturbances. It is shown that the forcing excites unstable disturbances relevant to the first and/or second mode of instability depending on the forcing frequency. The instabilities evolving through the separation region exhibits nontrivial behavior, which is not captured by 2D simulations. Distributions of the skin friction coefficient help to detect the beginning of LTT and estimate the length of transitional region. This study may help to setup and perform controlled experiments in quiet hypersonic wind tunnels.

2 Problem formulation and numerical method

2.1 Governing equations

The equations to be solved are the 3D unsteady Navier–Stokes equations in conservative dimensionless form. The fluid is a perfect gas with the specific heat ratio $\gamma = 1.4$ and Prandtl number $\mathrm{Pr} = 0.72$. The dynamic viscosity is calculated using Sutherland's formula $\mu = T^{3/2}(S+1)/(S+T)$, where $S = 110\,\mathrm{K}/T_\infty^*$. The second viscosity is assumed to be zero. The dependent variables are normalized to the corresponding freestream parameters: pressure – to the doubled dynamic pressure $\rho_\infty^* U_\infty^{*2}$; the coordinates – to the reference length L^* that is the distance from the leading edge to the corner point; time t – to L^*/U_∞^*. Hereafter asterisks denote dimensional quantities.

The details of the governing equations used for the DNS may be found in e.g. [16].

2.2 Numerical method

The Navier–Stokes equations are integrated using the in-house solver HSFlow (High Speed Flow), which implements an implicit finite-volume shock-capturing method with the second-order approximation in space and time. Godunov-type TVD scheme with Roe approximate Riemann solver is used. Reconstruction of dependent variables at the grid cell boundaries is performed using WENO (Weighted Essentially Non-Oscillatory) approach, which effectively gives the third-order space approximation. The system of nonlinear algebraic equations, which approximates the governing partial differential equations, is solved using the Newton iteration method. At every iteration step, the corresponding linear algebraic system is solved using the GMRes (Generalized Minimal Residual) method. Note that this approach is most efficient if the computational domain contains shock waves and other strong spatial inhomogeneities of the flow, such as boundary-layer separations. Despite dissipative nature of the TVD scheme, using the 2D HSFlow solver it was feasible to perform numerical simulations of boundary-layer receptivity and stability including configurations with separation bubbles [14, 16, 17].

The HSFlow solver employs MPI technology and PETSc framework for distributed calculations on a high-performance computing cluster. For parallel computations, the source structured grid is split up into multiple zones with one-to-one interzone connectivity. The discretization is done in each zone independently and fully parallel. The resulting algebraic equations are solved collectively by parallel methods implemented in PETSc library. The details on numerical method may be found in [18].

2.3 Flow parameters and computation domain

Computations are carried out for the flow over a 5.5° compression corner and flat plate at the freestream Mach number $M_\infty = 5.373$, the Reynolds number $\mathrm{Re}_\infty = L^* U_\infty^* \rho_\infty^* / \mu_\infty^* = 5.667 \times 10^6$, and temperature $T_\infty^* = 74.194\,\mathrm{K}$. The wall is isothermal with the surface temperature $T_w^* = 300\,\mathrm{K}$, $T_w = 4.043$. This configuration and flow parameters are the same as in [13, 14].

The boundary conditions are: no-slip condition $u = v = w = 0$ on the bottom ($y = y_{\min}$) boundary of computational domain; the free-stream conditions $u = 1$, $v = 0$, $p = 1/\gamma M_\infty^2$, $T = 1$ on the left ($x = x_{\min}$, inlet) and upper ($y = y_{\max}$) boundaries; the linear extrapolation from the interior for all the dependent variables on the right ($x = x_{\max}$, outlet) and front ($z = z_{\max}$) boundaries with $\partial^2(u, v, w, p, T) / \partial x^2 = 0$ and $\partial^2(u, v, w, p, T) / \partial z^2 = 0$, respectively; and the symmetry condition $\partial(u, w, p, T) / \partial z = 0$, $w = 0$ on the back ($z = z_{\min}$) boundary.

Computations are performed on a curved orthogonal grids with $2801 \times 221 \times 141$ nodes (86.24 million cells). The 2D grid for corner case with 2801×221 nodes (same as in [14]) is generated using numerical conformal mapping of a rectangle onto the computational domain. The grids is clustered near the surface so that 55% of nodes are within the boundary layer or

in the separation region including the mixing layer. Then a 3D grid is obtained by translating the 2D grid equidistantly.

2.4 Disturbances actuator

The problem is solved in two steps. First, a steady laminar flow field (basic flow) is computed using the time-dependent method. Then, unsteady disturbances are imposed onto the steady solution on the wall via the boundary condition for the vertical mass-flow perturbation

$$(\rho v)_w = \varepsilon \sin\left(2\pi \frac{x - x_1}{x_2 - x_1}\right) \sin\left(\pi \frac{z - z_1}{z_2 - z_1}\right) \sin\left(\omega_0 t\right)$$
,
$$x_1 \leq x \leq x_2,\ z_1 \leq z \leq z_2,\ 0 \leq t \leq t_1, \qquad (1)$$

where $x_1 = x_0 - d$, $x_2 = x_0 + d$, $z_1 = -d/2$, $z_2 = d/2$ are boundaries of the forcing rectangular region of the side ratio 2 with central point x_0 and size $d = 0.00815$. The forcing duration was chosen to be whether half of period $t_1 = \pi / \omega_0$ for wave packets generation, or infinity $t_1 = \infty$ for wave trains. To ensure linear evolution of the disturbances in the upstream region $x_0 < x < 1$, the forcing amplitude is chosen small, $\varepsilon = 10^{-3}$.

3. DNS results

3.1 Steady flow

Figure 1 shows near-wall fragments of the u-velocity fields computed on the flat plate and the compression corner. In the compression corner case, the boundary layer separates upstream of the corner point and reattaches somewhere downstream. Using the wall shear stress distributions, the coordinates of separation and reattachment points are detected as $x_{sep} = 0.857$ and $x_{att} = 1.136$, respectively. In between of these points, a shallow separation bubble is formed. The bubble contains a recirculation flow zone whose upper boundary is approximately a straight line that is typical for

supersonic separations. As expected, the boundary layer flows on a flat plate and the compression corner are very similar upstream of the separation point. More details on the basic (undisturbed) flow field can be found in [14].
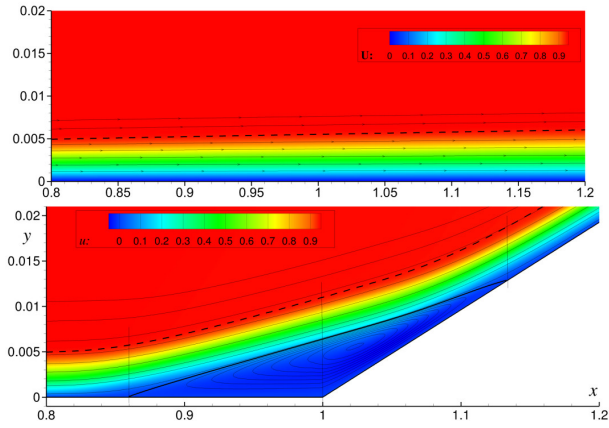

Fig. 1. The *u*-velocity field and streamlines in the boundary layer on the flat plate (upper) and on the compression corner (lower). Dashed line –boundary layer edge.

3.2 Simulation of wave packets

The wave packets are generated by a short pulse of suction-blowing actuator (1). Computations were performed at $\omega_0 = \omega_0^* L^* / U_\infty^* = 225$ corresponding to the frequency parameter $F_0 = \omega_0 / \mathrm{Re}_\infty = 3.97 \times 10^{-5}$. The pulse duration was $t_1 = \pi / \omega_0 = 0.014$. Such forcing has spectrum containing wide range of frequencies and wavenumbers, including plane high-frequency components relevant to the second-mode waves, as well as oblique low-frequency components associated with the first mode.

3.2.1 Forcing near leading edge

First we consider the case of forcing near the leading edge with actuator center point of $x_0 = 0.044$.

Fig. 2 illustrates the downstream propagation of the wave packet over the compression corner, where the instantaneous contours of the wall-pressure disturbance are shown at several time instances. Hereafter, the disturbance fields are obtained by subtracting the basic flow field from the fields at different time instances. The vertical lines indicate locations of the separation line $x_{sep} = 0.857$, the

corner line $x = 1$ and the reattachment line $x_{att} = 1.136$.

Initially the disturbance wave fronts emanating from the forced area are elliptic. As the disturbance propagates in the region upstream of separation, a V-shaped tail is formed while the wave-packet core exhibits a staggered 3D pattern. The packet is dominated by the oblique waves of $\omega \approx 100$ relevant to the first mode instability. The second-mode plane waves with relatively small amplitude and short wavelength are noticeable in the rear central part of the wave packet.
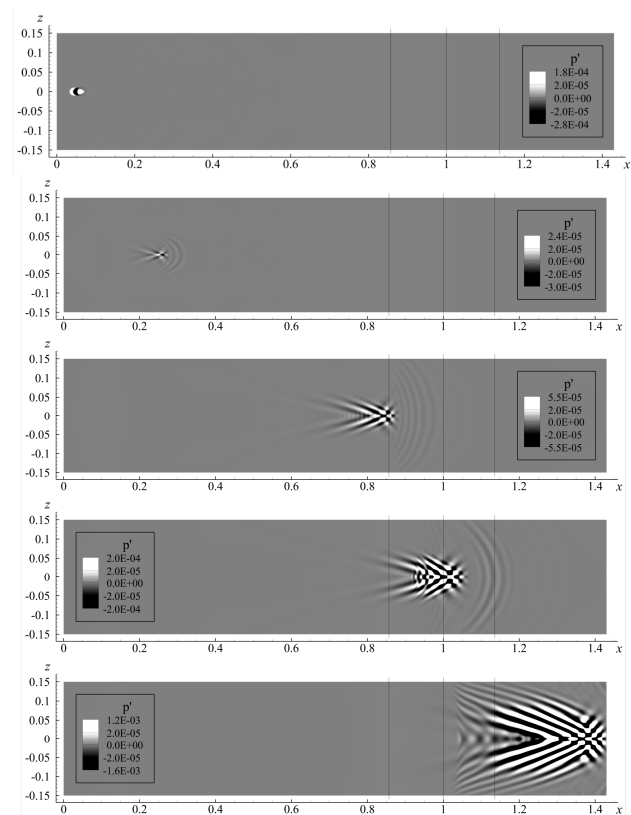

Fig. 2. Fields of corner wall-pressure disturbances at the time instants: $t = 0.025$; 0.25; 0.9; 1.1; 1.5. The forcing at $x_0 = 0.044$.

The wave packet crosses the separation line without noticeable changes of its structure. Further downstream, the wave packet quickly elongates in the streamwise direction. When its head reaches the reattachment point, the disturbance occupies more than one half of the separation region. As the wave-packet core propagates in the reattached boundary layer, the streamwise divergence is even stronger – the

fore part of disturbance moves faster than its rear part located in the separation region.

Figure 3 shows 3D vortical structures visualized at the time instance $t = 1.5$ using the Q-criterion. This pattern is typical for a wave packet containing oblique waves of the first-mode instability.
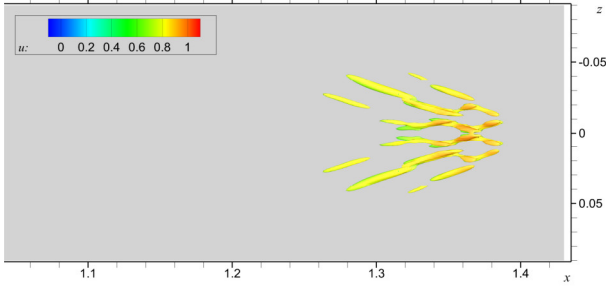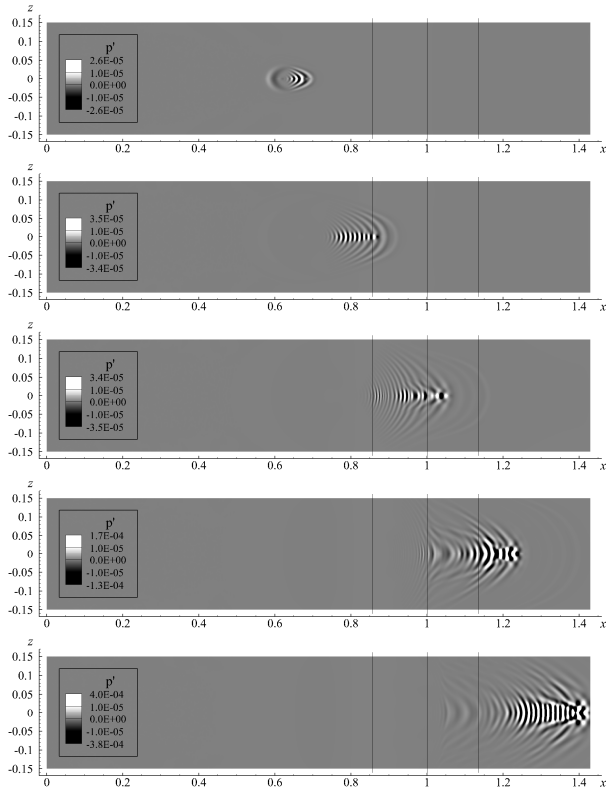

Fig. 3. Visualization of flow structures by isosurface of Q criterion at the time instance t = 1.5, Q = 100. Top view. The isosurface is colored using the u-velocity magnitude. The forcing at $x_0 = 0.044$.

3.2.2 Forcing far from leading edge

Fig. 4. Fields of corner wall-pressure disturbances at the time instants: t = 0.1; 0.3; 0.5; 0.7; 0.9. The forcing at $x_0 = 0.6$.

Now we consider the wave packet induced by the actuator with the central point $x_0 = 0.6$. In

this case, the major portion of the first-mode instability region is not involved, and the packet should be dominated by the second-mode plane waves.

Fig. 4 shows the disturbance at different time instants. The wave packet structures are qualitatively different from the previous case (Fig. 2). In the region upstream of the separation point, they resemble the second-mode dominated wave packet with plane waves in the core. As the wave packet propagates through the separation region, its 2D shape is preserved near the center line. When the wave packet leaves the separation bubble, its central part consists of plane waves associated with the second-mode instability of the reattached boundary layer.

The vortical structures visualized at the time instance $t = 0.8$ using the Q-criterion (Fig. 5) exhibit two-dimensional pattern typical for the second-mode instability. This is quite different from the previous case (Fig. 3).
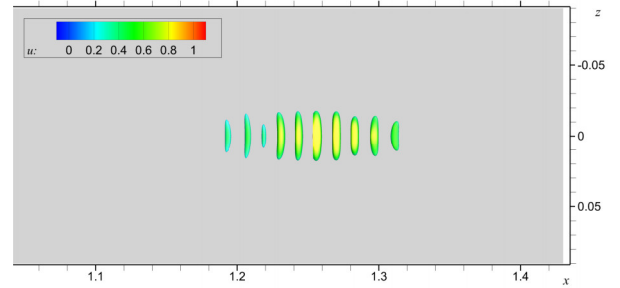

Fig. 5. Visualization of flow structures by isosurface of Q criterion at the time instance $t = 0.8$, Q = 5. Top view. The isosurface is coloured using the u-velocity magnitude. The forcing at $x_0 = 0.6$.

Thus, the wave-packet history strongly depends on where the initial disturbance is excited. At different streamwise locations of the actuator the wave packet can be first-mode or second-mode dominated that leads to qualitative changes of the disturbance history as well as its spectral content and spatial structure.

3.2.3 Strong forcing

Finally we consider stronger forcing at $\varepsilon = 10^{-2}$ (10 time higher amplitude) and $x_0 = 0.044$. Downstream the reattachment point a very young turbulent sport is formed that is illustrated by the visualization of flow structures using an isosurface of Q criterion (Fig. 6). Small-scale hairpin vortices fill up the central

portion of the wave packet surrounded by oblique waves, while the disturbance tail consists of longitudinal structures elongated downstream.
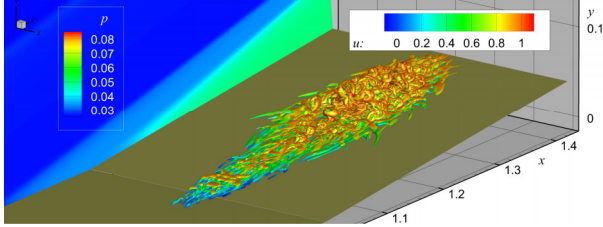

Fig. 6. Visualization of flow structures by isosurface of Q criterion at the time instance $t = 1.5$, $Q = 100$. The isosurface is colored using the u-velocity magnitude. The forcing at $\varepsilon = 10^{-2}$, and $x_0 = 0.044$.

More details on this numerical study can be found in [16].

3.2 Simulation of wave trains

The wave trains are generated by the suction-blowing actuator (1) working permanently with $t_1 = \infty$. Computations are performed at low frequency $\omega = 125$ associated with the first-mode instability, high frequency $\omega = 450$ associated with the second-mode instability and mid frequency $\omega = 225$. After transient process a three-dimensional wave train sets in the near-wall flow. In the linear stage, the wave train is harmonic with its frequency being equal to the forcing frequency at any fixed point in space. In the nonlinear breakdown stage, the disturbance evolves to a stationary stochastic state with its mean characteristics being constant versus time.

3.2.1 Wave trains of high frequency
First we consider wave trains generated at relatively high frequency $\omega = 450$ typical for the second-mode instability. Figure 7 shows instantaneous contours of the wall-pressure disturbance at $t = 2$.
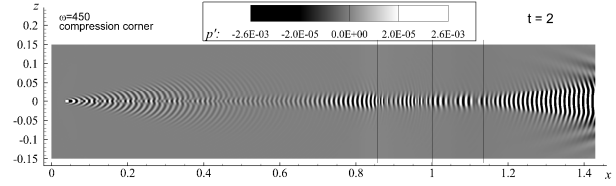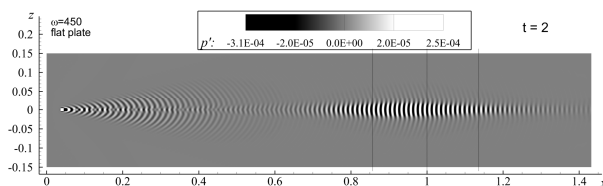

Fig. 7. Fields of the wall-pressure disturbance at $t = 2$ and $\omega = 450$. Flat plate (upper) and compression corner (lower).

In the region upstream of the separation point, the wave trains are almost identical and exhibit a 2D pattern typical for the second-mode instability. As the wave trains propagate further downstream, their behavior becomes different. In the flat plate case, the disturbance amplitude reaches its maximum at $x \approx 1$ and then decays. In the compression corner case, the wave train amplitude is modulated versus x in the separation region while its average level remains approximately constant; i.e., the separation bubble produces a stabilization effect on the second mode. This behavior agrees with the earlier results of 2D numerical simulations [13, 14].

Note that there is no appreciable spanwise diversion of the wave train in the separation region. Downstream from the reattachment point, the disturbance grows rapidly preserving its 2D structure.

Overall, these numerical simulations agree with the earlier stability and numerical studies [13-15] focused on the second-mode instability.

3.2.2 Wave trains of low frequency
Now we consider the wave trains generated at relatively low frequency $\omega = 125$ typical for the first-mode instability. Figure 8 shows instantaneous contours of the wall-pressure disturbance at a time instant $t = 1.7$. In the region upstream of the separation point, the wave train patterns are close to each other. Just behind the actuator they attain a V-shape typical for the first-mode dominated disturbance. As contrasted to the high-frequency case, their amplitude grows monotonically starting from the point $x \approx 0.075$. Near the central line, $z = 0$, the wave trains exhibit a staggered pattern which is surrounded by oblique waves from both sides.
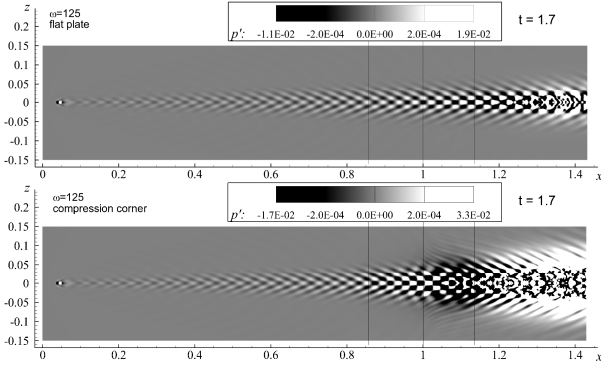
Fig. 8. Fields of the wall-pressure disturbance at $t = 1.7$ and $\omega = 125$. Flat plate (upper) and compression corner (lower).

Fig. 9. Fields of the wall-pressure disturbance at $t = 2.0$ and $\omega = 225$.

As the wave train propagates further downstream on the flat plate, its amplitude continues to grow and, ultimately, the nonlinear breakdown is observed behind the station $x \simeq 1.2$. In the compression-corner case the wave train quickly grows in the separation region. Its original structure starts to be distorted by nonlinear effects ahead of the reattachment point, and the disturbance becomes turbulent in the reattached boundary layer.

The separation leads to significant destabilization of the first-mode-dominated wave train.

3.2.3. Wave trains of mid frequency

Finally, we consider the wave train of mid frequency $\omega = 225$. Figure 9 shows instantaneous contours of the wall-pressure disturbance at a time instant $t = 2$. The growth is weaker than in the low-frequency case. The mid-frequency wave train evolves linearly throughout the computational domain.

In the fore part of separation bubble ($x_{sep} < x < 1$), the disturbance pattern spreads out and transforms into Y-shape. However, in the rear part ($1 < x < x_{att}$) the pattern returns to its typical V-shape.
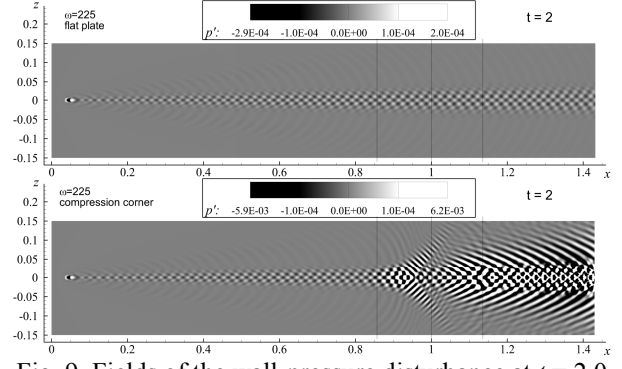
To explore these new features we consider three-dimensional eddies snapshot (Fig. 10). The disturbance field splits into several layers: 1) In the near-wall layer there are oblique waves propagating away from the central line at a relatively large angle. Their footprint on the wall gives the Y-shape pattern in the mid part of separation bubble. 2) In the mid (mixing) layer, the vortical structures are typical for the first-mode dominated wave train. 3) In the outer layer (above the separation bubble) there are pressure waves radiated from a near-wall region located between the separation and corner points.
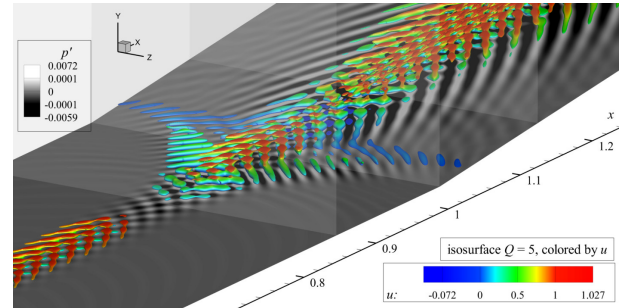

Fig. 10. Vortical structures in the separation bubble at $t = 2$ and $\omega = 225$. The structures are visualized using the isosurface of Q=5 coloured by the u-velocity magnitude. Grey semi-transparent slices show x-stations of separation, corner and reattachment. Black and white pattern shows the pressure disturbance footprint on the wall.

More details on this wave trains simulation can be found in [19].

4 Conclusions

Three-dimensional wave packets and trains propagating over a 5.5 degree compression corner and a flat plate at the freestream Mach

number M_∞ = 5.373 were investigated using direct numerical simulations. Unsteady three-dimensional compressible Navier–Stokes equations were integrated using an implicit finite-volume shock-capturing method with the second-order approximation in space and time. The problem was solved in two steps. First, a steady laminar flow field (basic flow) was computed using a time-dependent method. Then, the unsteady disturbances are imposed onto the steady solution using small suction-blowing actuator modelled by the local in space forcing of the vertical mass-flow on the wall. The forcing was applied whether for short time or permanently.

The short time working actuator generate a broad spectrum of waves including the first-mode and second-mode instabilities. The suction-blowing pulse develops into a three-dimensional wave packet propagating downstream.

In the case with the actuator located near the leading edge, the wave packet is dominated by oblique waves of relatively low frequency which are relevant to the first mode.

If the actuator is located far downstream of the leading edge so that the major portion of the first-mode instability region is not involved, the wave packet is dominated by the second mode. The disturbance remains neutral in the fore part of separation region $x_{sep} < x < 1$. Further downstream the wave packet grows with appreciable rate.

Thus, the wave-packet history strongly depends on how and where the initial disturbance is excited, i.e., the role of receptivity is crucial. At different streamwise locations of the actuator, the wave packet can be first-mode or second-mode dominated that leads to qualitative changes of the spectral content and spatial shape of the disturbance.

The permanently working actuator generate a wave train of fixed frequency. The separation bubble produces a stabilization effect on the high-frequency wave train related to the second mode. The wave-train amplitude is modulated in the streamwise direction while its

average level remains approximately constant in the separation region. Downstream from the reattachment point, the disturbance grows rapidly preserving its 2D structure.

In the low-frequency case, separation leads to significant destabilization of the wave train dominated by the first-mode instability. The disturbance quickly grows in the separation region, exhibits nonlinear behavior ahead of the reattachment point, and becomes turbulent in the reattached boundary layer.

In the mid-frequency case, where 2D and 3D waves are equally important, the wave train behavior is abnormal within the separation bubble. The disturbance field splits into several layers: 1) In the near-wall layer there are oblique waves propagating away from the central line at a relatively large angle. Their footprint on the wall gives the Y-shape pattern in the mid part of separation bubble. 2) In the mid (mixing) layer, the vortical and pressure-disturbance structures are typical for the first-mode dominated wave train. 3) In the outer layer (above the separation bubble) there are pressure waves radiated from a near-wall region located between the separation and corner points.

In the mid-frequency case, the separation bubble supports not just one mode but, presumably, several modes of different nature. The interference between plane (2D) and oblique (3D) wave-components of these modes leads to intricate spatial structures which are not observed in the low frequency and high-frequency cases.

These numerical examples demonstrate that supersonic separation strongly affects boundary-layer instabilities in different ways depending on the frequency content of unstable disturbances.

This and similar numerical simulations will help to setup and perform controlled experiments in quiet hypersonic wind tunnels as well as develop holistic models of transitional boundary layer at hypersonic speeds.

5 Acknowledgments

References

[1] Fedorov A. Transition and Stability of High-Speed Boundary Layers. *Annu. Rev. Fluid Mech.*, Vol. 43, pp. 79-95, 2011.

[2] Kosinov A. D., Semionov N. V., Shevelkov S. G. and Zinin O. I. Experiments on the nonlinear instability of supersonic boundary layers. In *Nonlinear Instability of Nonparallel Flows*. Springer, pp. 196–205, 1994.

[3] Kosinov A. D. and Tumin A. Resonance interaction of wave trains in supersonic boundary layer. In *Nonlinear Instability and Transition in Three-Dimensional Boundary Layers*. Kluwer Academic Publishers, pp. 379–388, 1996.

[4] Laddon D.W. and Schneider S. P. Measurements of controlled wave packets at Mach 4 on a cone at angle of attack. AIAA-1998-0436, 1998.

[5] Shiplyuk A. N., Bountin D. A., Maslov A. A. and Chokani N. Nonlinear mechanisms of the initial stage of laminar-turbulent tansition at hypersonic velocities. *J. Appl. Mech. Tech. Phys.*, Vol. 44, No. 5, pp. 1–12, 2003.

[6] Bountin D., Shiplyuk A. and Maslov A. Evolution of nonlinear processes in a hypersonic boundary layer on a sharp cone. *J. Fluid Mech.*, Vol. 611, pp. 427–442, 2008.

[7] Casper K.M., Beresh S.J., and Schneider S.P. Pressure fluctuations beneath turbulent spots and instability wave packets in a hypersonic boundary layer. AIAA paper 2011-372, 2011.

[8] Casper K., Beresh S. and Schneider S. Characterization of controlled perturbations in a hypersonic boundary layer. AIAA paper 2012-281, 2012.

[9] Chou A. and Schneider S.P. Time-Frequency Analysis of Boundary Layer Instabilities Generated by Freestream Laser Perturbations. AIAA paper 2015-3076, 2015.

[10] Zhong X. and Wang X. Direct Numerical Simulation on the Receptivity, Instability, and Transition of Hypersonic Boundary Layers. *Annu. Rev. Fluid Mech.*, Vol. 44, pp. 527-561, 2012.

[11] Fasel H.F. Numerical Simulation of Transition in Hypersonic Boundary Layers. AFRL-OSR-VA-TR-2012-0255, AFOSR/RSA, 2011.

[12] Berry S.A., DiFulvio M. and Kowalkowski M.K. Forced Boundary Layer Transition on X-43 (Hyper-X) in NASA LaRC 20-Inch Mach 6 Air Tunnel. NASA TM-2000-210316, 2000.

[13] Balakumar P., Zhao H. and Atkins H. Stability of hypersonic boundary layers over a compression corner. *AIAA J.*, Vol. 43, No. 4, pp. 760-767, 2005.

[14] Egorov I.V., Novikov A.V. and Fedorov A.V. Numerical modeling of the disturbances of the separated flow in a rounded compression corner. *Fluid Dynamics*, Vol. 41, No. 4, pp. 521–530, 2006.

[15] Zhao H. and Balakumar P. Nonlinear disturbance evolution across a hypersonic compression corner. *AIAA J.*, Vol. 43, No. 5, pp. 1034-1041, 2005.

[16] Novikov A., Egorov I and Fedorov A. Direct numerical simulation of wave packets in hypersonic compression-corner flow. *AIAA J.*, Vol. 54, No. 7, pp. 2034-2050, 2016.

[17] Bountin D., Chimitov T., Maslov A., Novikov A., Egorov I., Fedorov A. and Utyuzhnikov S. Stabilization of a hypersonic boundary layer using a wavy surface. *AIAA J.*, Vol. 51, No. 5, pp. 1203-1210, 2013.

[18] Egorov I.V. and Novikov A.V. Direct numerical simulation of laminar–turbulent flow over a flat plate at hypersonic flow speeds. *Computational Mathematics and Mathematical Physics*, Vol. 56, No. 6, pp 1048-1064, 2016.

[19] Novikov A., Fedorov A. and Egorov I. Numerical study of wave trains in supersonic flow over a compression corner. AIAA paper 2016-0049, 2016.

8 Contact Author Email Address

AndrewNovikov@yandex.ru

Copyright Statement